Hydrogen Bubbles and the Growth Morphology of Ramified Zinc by Electrodeposition

Article *in* Journal of The Electrochemical Society · January 2008

DOI: 10.1149/1.2894189 · Source: OAI

Journal of The Electrochemical Society, **155** (5) D400-D407 (2008)
0013-4651/2008/155(5)/D400/8/$23.00 © The Electrochemical Society

Hydrogen Bubbles and the Growth Morphology of Ramified Zinc by Electrodeposition

Pei-Cheng Hsu,[a,b] Seung-Kwon Seol,[c] Tsung-Nan Lo,[a] Chi-Jen Liu,[a] Chang-Liang Wang,[a] Chao-Sung Lin,[b,*] Y. Hwu,[a,d,e,f,z] C. H. Chen,[g] Liu-Wen Chang,[h] J. H. Je,[c] and G. Margaritondo[i]

[a]*Institute of Physics, Academia Sinica, Taipei 115, Taiwan*
[b]*Department of Materials Science and Engineering, National Taiwan University, Taipei 106, Taiwan*
[c]*X-ray Imaging Center, Pohang University of Science and Technology, Pohang, Korea*
[d]*Department of Engineering Science and System, National Tsing Hua University, Hsinchu, Taiwan*
[e]*Institute of Optoelectronic Sciences, National Taiwan Ocean University, Keelung, Taiwan*
[f]*National Synchrotron Radiation Research Center, Hsinchu 300, Taiwan*
[g]*Kuan Tai Metal Technology Incorporated, Tainan, Taiwan*
[h]*Institute of Materials Science and Engineering, National Sun Yat-Sen University, Kaohsiung, Taiwan*
[i]*Ecole Polytechnique Fédérale de Lausanne, CH-1015 Lausanne, Switzerland*

Real-time X-ray microscopy was used to study the influence of hydrogen-bubble formation on the morphology of ramified zinc electrodeposit. The experimental results show that when intense hydrogen bubbling occurs at high potential, the morphology of the ramified zinc deposit changes from dense-branching to fern-shaped dendrite. The fern-shaped dendrite results in part from the constricted growth due to hydrogen bubbles but also from the highly concentrated electric field. The fern-shaped dendrite morphology was observed during the early stages of electroplating for both the potentiostatic and galvanostatic modes; however, the deposit plated in the galvanostatic mode densified via lateral growth during the later plating stages. This indicates that potentiostatic plating for which the hydrogen-bubble formation steadily occurs throughout the electrodeposition process is better than galvanostatic plating for fabricating fern-shaped deposits, which are ideal electrodes for Zn–air batteries due to the relatively large specific area.
 [DOI: 10.1149/1.2894189]

Manuscript submitted December 27, 2007; revised manuscript received February 5, 2008.
Available electronically March 20, 2008.

Hydrogen-bubble formation is a well-known phenomenon during metal electrodeposition and is normally considered a nuisance because of its negative impact on the quality of the deposit.[1,2] However, one can also take advantage of the bubbles. For example, it was realized that the surface of the bubble can provide active sites for zinc electrocrystallization.[3] Hydrogen bubbles can also serve as a dynamic template for fabricating self-supporting three-dimensional foams of metal deposit.[4] Along these lines, we demonstrate here that hydrogen bubbles directly affect the growth morphology and can make it possible to control the dendritic growth as required for certain important applications.

Electrodeposition is one of the main techniques to fabricate ramified structures with high surface areas,[5-9] in particular with zinc. In turn, zinc electrodes are widely used in battery systems. To enhance the battery efficiency, zinc electrodes with high surface areas are preferable. A wide variety of ramified Zn deposit patterns can be obtained by varying the growth conditions.[10-12] For example, Lopez and Choi[13] studied zinc dendrite morphologies electroplated in nonaqueous formamide media. Their results indicate that the morphological features of dendrite zinc electrodes, such as particle size, shape, and degree of branching, markedly influence the physical, chemical, and electrochemical properties. However, a detailed understanding of the electrochemistry and physics of the ramified growth[14-18] has been limited so far by the lack of suitable monitoring tools.

We attacked this problem using the high speed and high resolution of phase-contrast microradiology[19-23] with synchrotron X-rays. Phase contrast particularly makes the detection of the small difference in the X-ray refractive index between air and liquid possible and facilitates the otherwise impossible imaging of bubble evolution by X-ray microscopy. The other less-obvious benefit introduced by the use of phase contrast is to allow microradiology observation at a much greater distance from the specimen without suffering image degradation from edge blurring. With the high penetration and the high brightness of synchrotron hard X-ray, phase-contrast microradiology enabled us to investigate in detail the hydrogen-bubble formation process and the corresponding electrodeposition morphology in three-dimension (3D) and in a standard environment.[24,25] We observed morphological transitions of the ramified zinc deposits plated under both the galvanostatic and potentiostatic modes that are clearly linked to the presence of hydrogen bubbles.[3,19,20]

Specifically, our approach enabled us to quantitatively measure the hydrogen-bubble formation and assess its dependence on the applied potential and its impact on consequent morphology of the deposit.[26] Conventional studies of this problem would require the macroscopic analysis of the growth morphology, removal of the deposit from the electrolyte for microanalysis, and calculations of the metal plating efficiency, with qualitative information on bubble formation. This approach, without real-time in situ observation, would miss the important morphology transitions and their link to hydrogen-bubble formation.

The observed morphology change from dense-branching[27,28] to fern-shaped dendrite in the potentiostatic plating mode with increasing potential was found to be directly related to increased hydrogen-bubble formation. The hydrogen bubbles also affected the ramified growth in galvanostatic plating. In this case, however, lateral growth was found to occur during the later plating stages when the effect of the hydrogen bubbles decreased.

Among these morphologies, the fern-shaped dendrite has the highest surface area and can be of practical use in batteries if its growth can be controlled as indicated by our results. Therefore, our findings have a potential impact on applications besides explaining the plating-growth dynamics, leading to different morphologies.

Previous real-time studies of ramified electrodeposit formation were performed in two-dimensional (2D) cells due to the depth-of-focus problem while using optical microscopy. The role of hydrogen bubbles was not a main objective of these studies, because in 2D electroplating cells the bubbles markedly retard the development of ramified electrodeposits. Our experimental approach enabled us to monitor hydrogen-bubble evolution and the related Zn deposit morphological changes in 3D and with no restrictions on the elec-

* Electrochemical Society Active Member.
[z] E-mail: phhwu@sinica.edu.tw

trodeposition geometry. This made it possible to discover bubble effects that are potentially positive rather than negative, specifically for obtaining metal electrodes with large surface areas.[29-34]

Experimental

Zinc electrodeposits were grown in either the potentiostatic (constant potential) mode or the galvanostatic (constant current) mode at room temperature in an aqueous solution composed of 2.2 M $ZnCl_2$ and 4.8 M KCl without stirring. The electrolyte was prepared with analytical chemicals and deionized water and deaerated with bubbling nitrogen prior to electroplating.

A three-electrode electrochemical cell was specifically designed for our in situ microradiography experiments. The cell was machined from Teflon bulk and had two windows with adjustable positions to control the solution thickness. In the experiments discussed here, a 5 mm thick solution was selected so as to avoid unnecessarily excessive X-ray absorption by the electrolyte while providing adequate space for ramified growth. The distance between the cathode and anode was adjusted to 10 mm. The working electrode was made of copper rod, had a cross-sectional area of 0.5 $\times$ 2 mm^2, and was embedded in corrosion-resisting epoxy. Before each run, the electrode was polished with 2400 grit emery paper, cleaned in a 5% sulfuric acid solution for 5 s, and finally rinsed with deionized water. The counter electrode was an electrolytic zinc plate, and the reference electrode was a saturated calomel electrode (SCE) positioned close to the working electrode using a Luggin capillary. Electroplating was performed using an Autolab PGSTAT 30 potentiostat/galvanostat. All potentials reported in this article are with respect to the SCE. During electroplating, microradiography with coherent X-rays was performed in real time using the 01A beamline of the National Synchrotron Radiation Research Center, Taiwan and the 7B2 beamline of the Pohang light source, Korea.[35]

In order to explain the growth dynamics, the electric-field distribution across zinc anode and copper cathode was calculated with the ANSYS software based on the assumption that the electrolyte composition is uniform and the solution electrical receptivity remains constant during electroplating.

Results and Discussion

It is well documented that the common "well-defined morphologies," such as diffusion-limiting aggregation, dense-branching morphology, and dendrite morphology,[10,11,27,28] cannot be obtained in a 2D electrodeposition cell when hydrogen bubbles are developed together with the ramified growth.[36] When hydrogen bubbles are generated in a 2D cell, the deposition is retarded or jeopardized and spongy deposits are usually formed instead of a well-defined morphology. However, a well-defined morphology often does coexist with hydrogen bubbles in 3D environments.[4]

As already mentioned, the reason for performing experiments in 2D is the use of optical microscopy. Although laser confocal microscopy has better imaging capabilities for thicker specimens, it has a relatively slow imaging speed not suitable for real-time electrodeposition studies. Furthermore, when hydrogen bubbles are formed they interfere with optical microimaging, making it difficult to observe their effects.

Studies in 2D are arguably simpler than those in 3D, because they are not affected by complications like convection and, indeed, hydrogen bubbles. We believe, however, that due to progress in the knowledge of electrodeposition, 3D studies are now justified and timely. The high penetration of X-ray microscopy enabled us to make the transition from 2D to 3D.

We first measured the cathodic-polarization curves to determine the basic electrochemical parameters of this system. The results of the polarization-curve measurement at a few example scanning rates are shown in Fig. 1. The detailed differences as shown in the inset highlight the problem of such measurements in providing the fundamental electrochemical properties of the electrolyte, because the changes in the electrode surface and morphology in the case to study

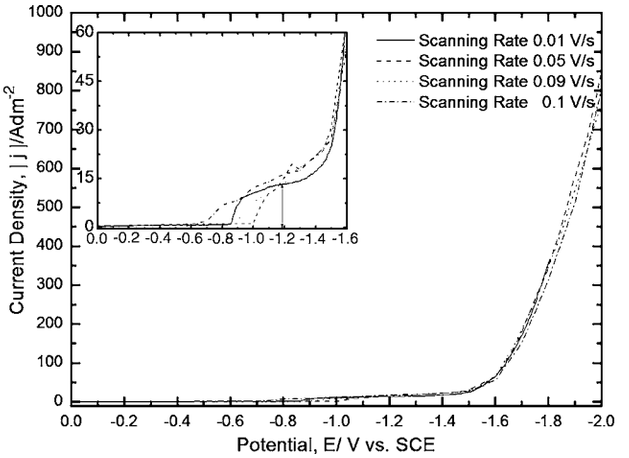

Figure 1. The cathodic polarization curves of zinc electrodeposition under different scanning rates.

dendritic growth can no longer be ignored. We therefore use apparent current density to reflect the fact that we are handling an unfixed electrode.

In our case, after the onset of the deposition, there is a clear difference in the cathodic-polarization curves scanned at different rates. However, the common characteristics (the sharp rise in the apparent current density at potential >1.5 V) is almost identical. It is well known that this rise is a direct sign of the electrolysis of water and the consequential formation of hydrogen bubbles. To ensure that our study is not affected by the variation in cathode morphology, we monitor the electrode in real time during the measurement of the cathodic-polarization curve.

Figures 2 and 3 show an example of the simultaneously measured cathodic-polarization curve at a rather fast scan rate of 0.09 V/s and X-ray radiographs showing the morphological evolution. Zinc plating is not observed at the potential period of 0 to -1.0 V (Fig. 3a and b). The formation of a compact layer is at the region with potential ca. -1.0 V (Fig. 3c). This is quite reasonable compared to the standard reduction potential of zinc at -0.76 V vs standard hydrogen electrode (-1.0 V vs SCE). Due to the high scanning rate, the detail of morphological evolution is not monitored closely. However, dendritic growth is observed (Fig. 3d and f), which explains that the variation of the polarization curves at different scanning rates is indeed related to the changing morphology of

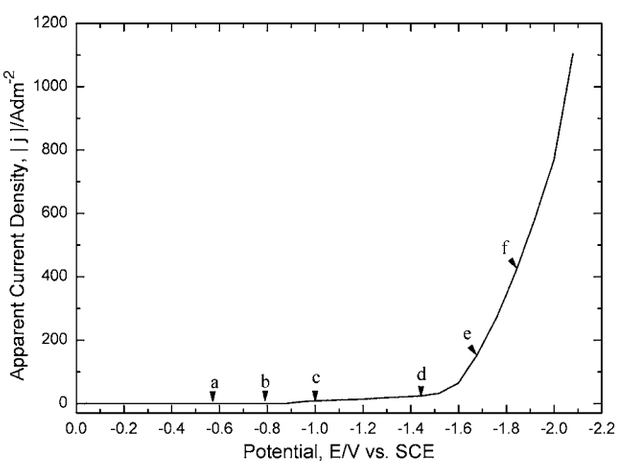

Figure 2. A cathodic polarization curve at a scan rate of 0.09 V/s.

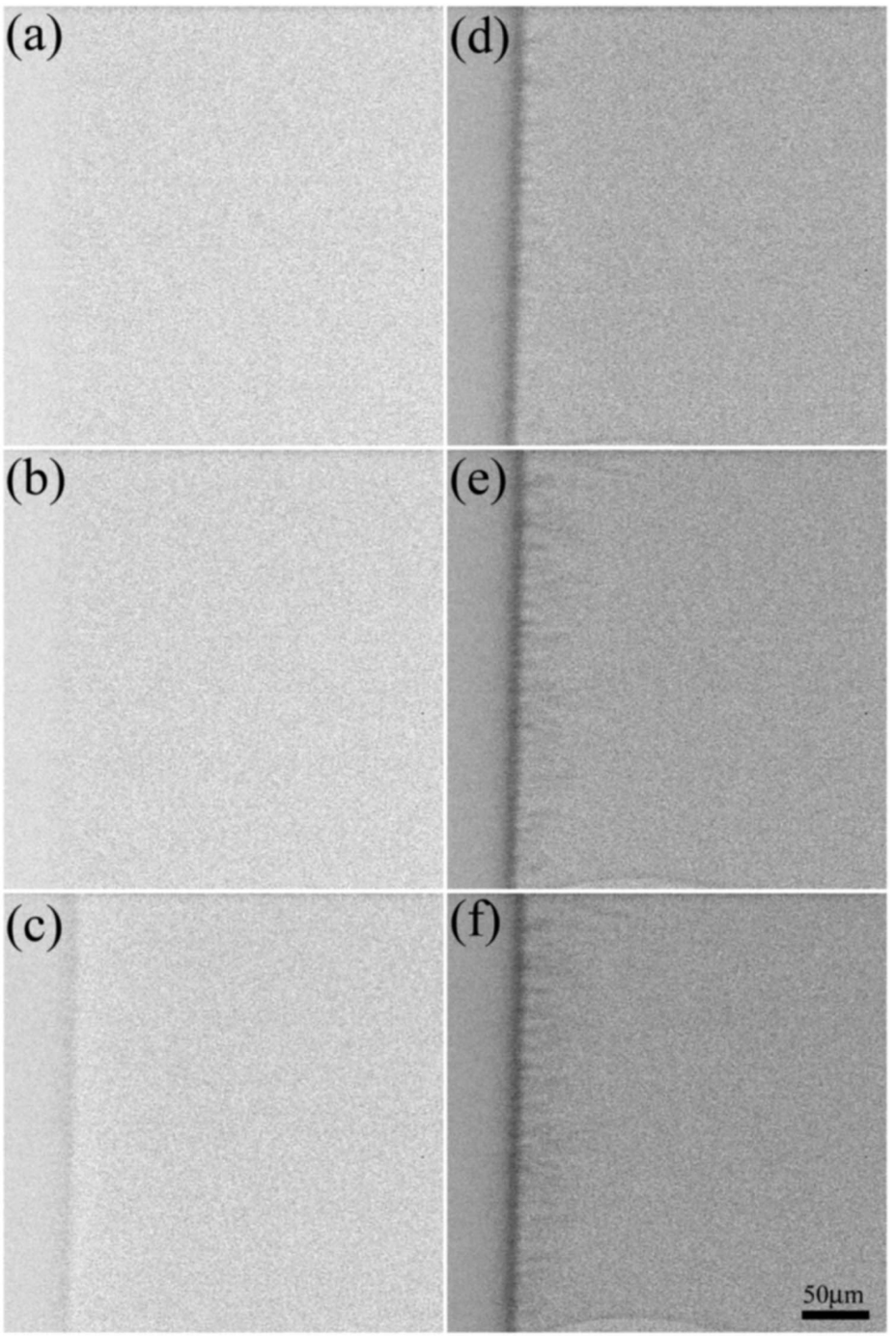

Figure 3. Sequence of microradiographs showing the morphological evolution during cathodic polarization scanning.

the deposit. Dendritic growth does not appear with zinc electroplating before the ramping up of the potential reaches the end of this type of fast scans.

In addition to the fast rising in the apparent current density at higher potential, a plateau in the polarization curve can still be qualitatively derived. For example, such an obvious plateau in Fig. 1 was observed at ~ 13 A dm^{-2} and identified as the limiting current density[37] determined by the maximum rate of mass transfer by diffusion. When the negative potential is higher than this plateau region, intense hydrogen-bubble formation was indeed observed dominating the electrochemical reaction, and the clear threshold, as seen in Fig. 1, indicated the onset of water electrolysis.

To analyze the effects of the electrode changes, we extracted the peak voltage in the galvanostatic measurements, such as those plotted in Fig. 4a, at different current densities; the results are plotted in Fig. 4b. These peak voltages obtained in the galvanostatic mode right after turning on the current provide a good picture of the voltage–current density characteristics for a clean surface. The results again show a plateau at a current ~ 13 A dm^{-2}. Therefore, the limiting current density obtained with this approach is in agreement with that obtained from Fig. 1.

Real-time X-ray microscopy measurements confirm that with higher voltage and current densities intense bubble formation starts.

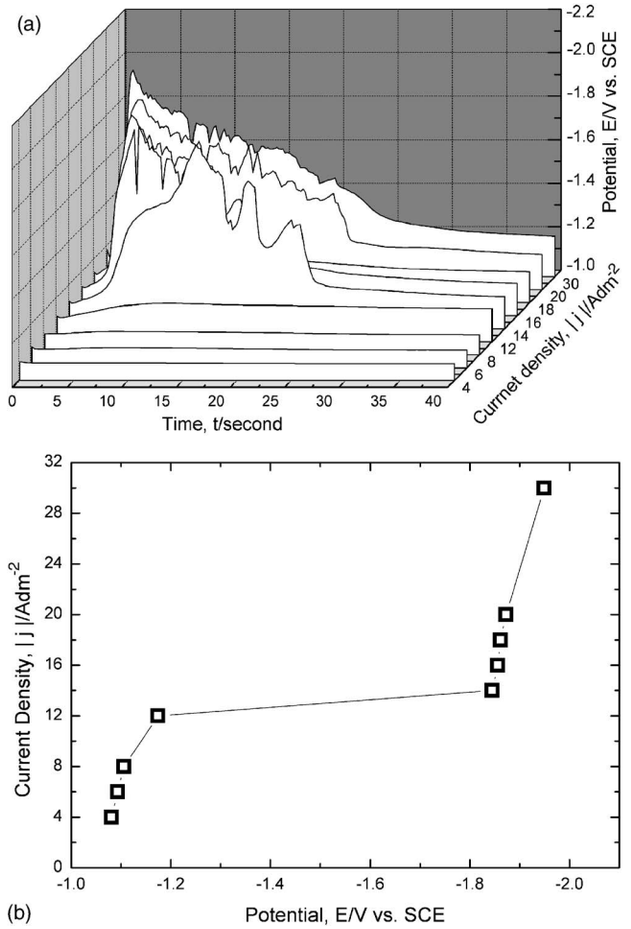

Figure 4. (a) The voltage–time curve measured at different current densities. (b) The extracted peak voltage in (a) plotted as a function of the current density.

In fact, the level-off voltage, ca. −1.2 V in Fig. 4a, or the threshold voltage of −1.5 V in Fig. 1, which is consistent with the electrolysis potential of water for the cathodic electrode,[38] is a more relevant parameter than the limiting current density because it corresponds to the onset of the hydrogen-bubble formation. Our investigations of the effect of bubbles on ramified growth were mostly focused on this regime of intense bubble formation.

A small number of hydrogen bubbles can already be observed during zinc electrocrystallization in conditions near the limiting current density region. Figure 5 shows an example of galvanostatic deposit plated at 13 A dm^{-2}. A dense-branching structure grew linearly with the electroplating time. The formation of hydrogen bubbles does not appear to affect the ramified growth, and the deposit became denser as electroplating continued. A similar growth behavior was observed in the potentiostatic deposition mode at low potential. Therefore, this appears as the growth morphology in the absence of bubble effects.

Above the limiting current density region, the cathode reaction was dominated by the creation of hydrogen bubbles; simultaneously, a morphological transition was observed during the ramified growth. Sequential microradiographs of the deposit plated in the galvanostatic mode at 20 A dm^{-2} are shown in Fig. 6. In the early stages of electroplating, most of the cathode surface was covered by hydrogen bubbles, leaving a limited number of spots available for deposit nucleation and limited directions for deposit growth. A fern-shaped dendrite was formed and consisted of a main stem, around which many side branches were uniformly distributed.

The fern-shaped structure grew outward within a short period of time (Fig. 6a-c), producing a completely nucleated structure before lateral growth prevailed at a rate significantly higher than that of the outward growth. Overall, the fern-shaped dendrite morphology gradually disappeared and a dense deposit formed with top-heavy characteristics (Fig. 6d-h).

The electrostatic potential was measured in situ during galvanostatic electroplating like that of Fig. 4. Figure 7a shows a potential transient curve at 20 A dm^{-2}. The curve can be divided into three stages: when the current was switched on, the voltage immediately rose to a given value, then drastically dropped over a few seconds and decreased more gradually afterward. These stages correspond to the transitions in the electrode conditions.[39]

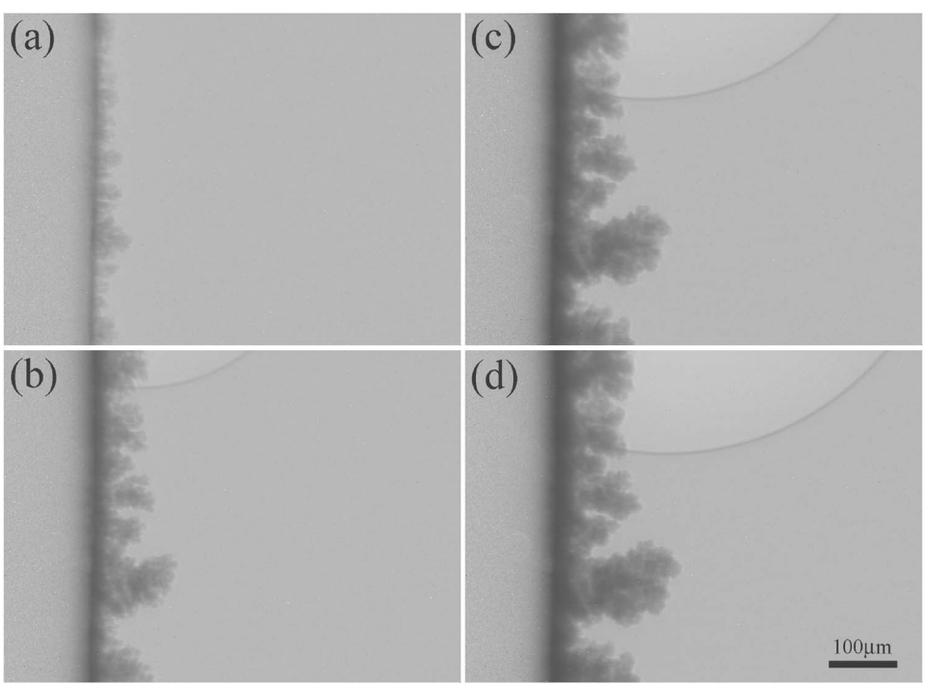

Figure 5. Sequential microradiographs of dense-branching growth at 13 A dm^{-2}, taken at different times during growth: (a) 99, (b) 255, (c) 411, and (d) 515 s.

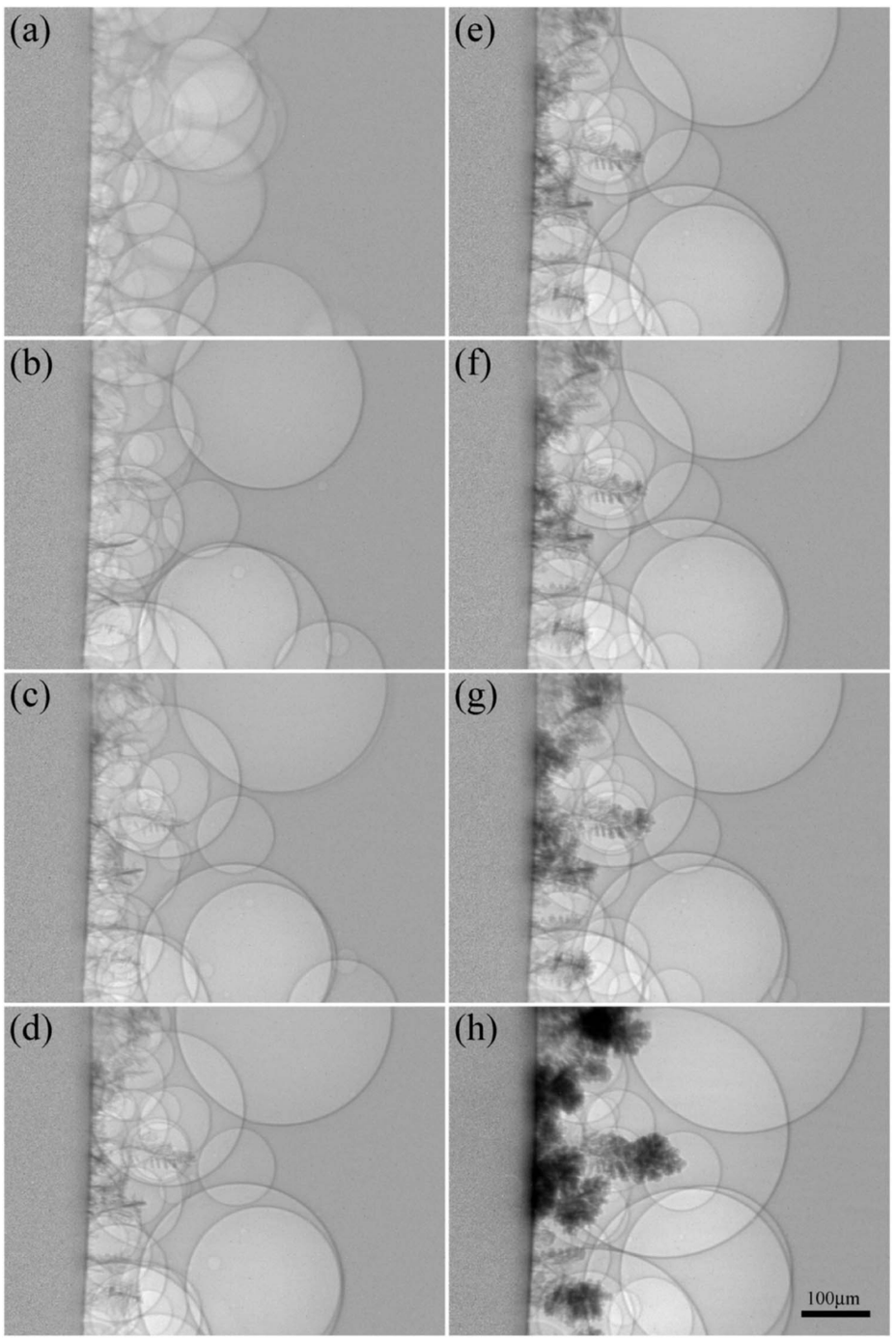

Figure 6. Sequence of microradiographs showing a zinc deposit on a copper substrate (on the left) obtained with galvanostatic plating at 20 A dm^{-2}. The images correspond to the times (a) 5.4, (b) 10.6, (c) 15.8, (d) 21, (e) 26.2, (f) 31.4, (g) 47, and (h) 151 s. Images (a-d) show that the deposited zinc forms fern-shaped dendrites with outward growth, whereas images (e-h) show dense-branching dendrites with lateral growth.

The first stage was associated with the double-layer charging, when the conductivity of the electrolyte went to zero as the concentration of zinc ions became negligible at the cathode. After the maximum voltage, a linear decrease in voltage with the plating time was noted along with the appearance of fern-shaped dendrites. Such a decrease, occurring instead of the expected steady voltage, is caused by the evolution of the deposit. Indeed, the ramified structure increases the cathodic surface area and therefore reduces the potential at constant current. Strong hydrogen-bubble formation interfered with the potential measurements, leading to voltage oscillation during the second stage. During the final stage, the voltage gradually decreased to ca. −1.2 to −1.0 V, and hydrogen-bubble creation nearly terminated. The potential measurements yielded smooth curves without oscillations.

We found that the potential of the final stage in the potential transition curves was always −1.2 to −1.0 V in the region above limiting current density. Experiments performed with a current density of 30 A dm^{-2} yielded the same trend in the potential (Fig. 7b). For all current densities, the last growth stage results in a dense branching morphology instead of an outward growth, developed by lateral growth of the fern-shaped dendrites.

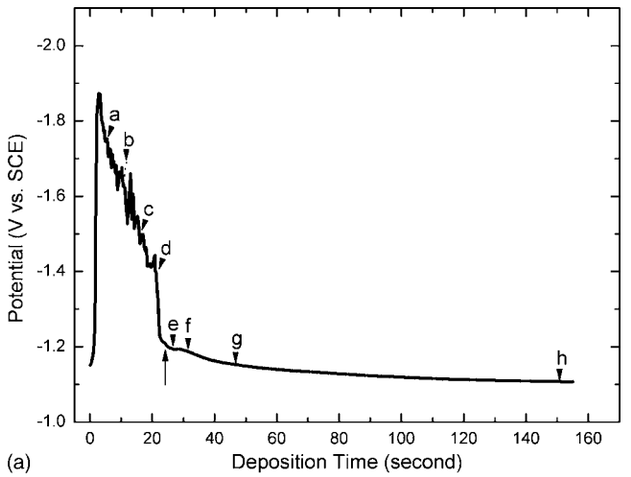

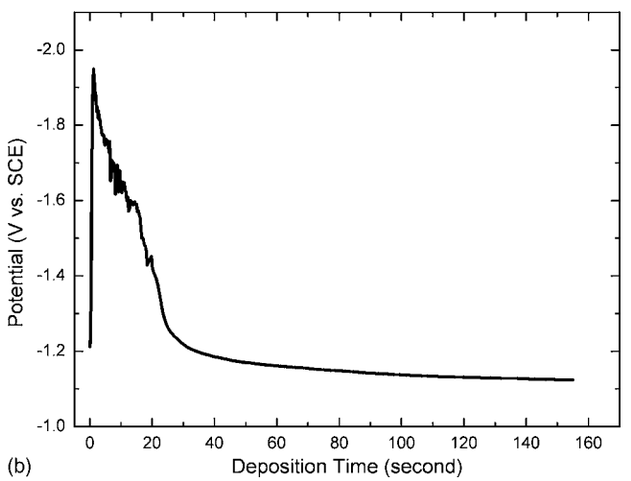

Figure 7. (a) Potential transient curve at 20 A dm^{-2}. The arrow labeled a-h corresponds to the microradiographs in Fig. 3. (b) Potential transient curve at 30 A dm^{-2}.

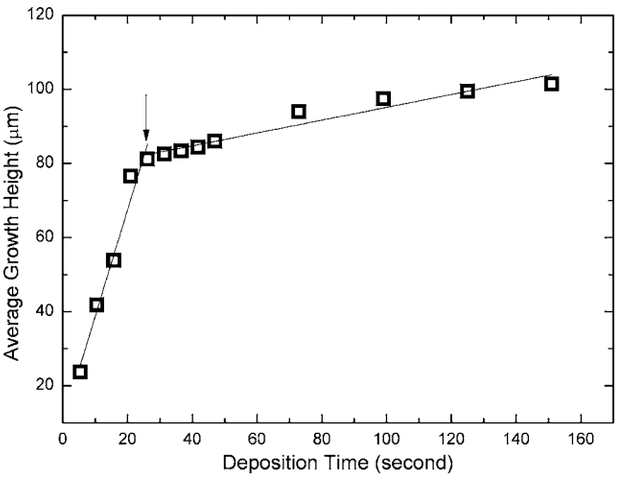

Figure 8. The average growth height vs deposition time galvanostatic plating at 20 A dm^{-2}.

Figure 8 shows the average growth height (measured from the substrate/deposit interface to the deposit surface) as a function of electroplating time at 20 A dm^{-2}. The fern-shaped dendrites generally grew faster than dense-branching deposits regardless of the current density. The average growth height of the fern-shaped dendrites increased linearly with time when the outward growth prevailed. The growth rate of the fern-shaped dendrite decreased dramatically at the transitional point (the arrow in Fig. 8), and a smaller growth rate was observed afterward for the dense-branching deposit. This rate change coincides precisely with the slope change of the potential transient curve, marked by the arrow in Fig. 7a, confirming again the strong correlation with hydrogen-bubble formation.

Figure 9 shows an example of zinc electrocrystallization at an applied potential of −1.8 V that is well above the limiting current density region; the hydrogen-bubble effects dominate the deposition, and fern-shaped dendrites are formed. Unlike the galvanostatic

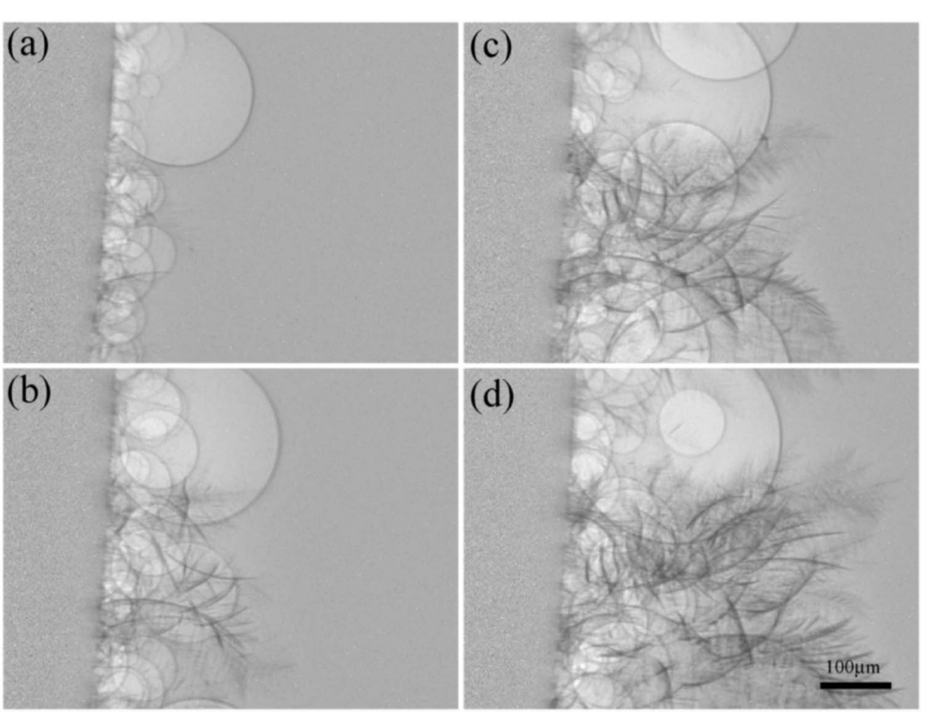

Figure 9. Sequential microradiographs of fern-shaped dendrites growth at −1.8 V, taken at different times: (a) 5.4, (b) 10.6, (c) 15.8, and (d) 21 s.

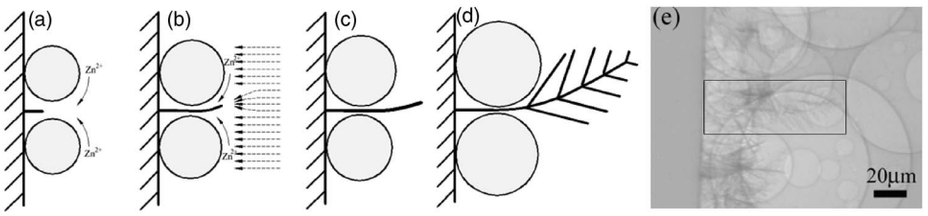

Figure 10. Schematic diagram showing the formation of fern-shaped dendrites. The circles indicate hydrogen bubbles. The dotted arrowhead lines indicate the electric field. The main stem of the fern-shaped dendrite grows between two hydrogen bubbles.

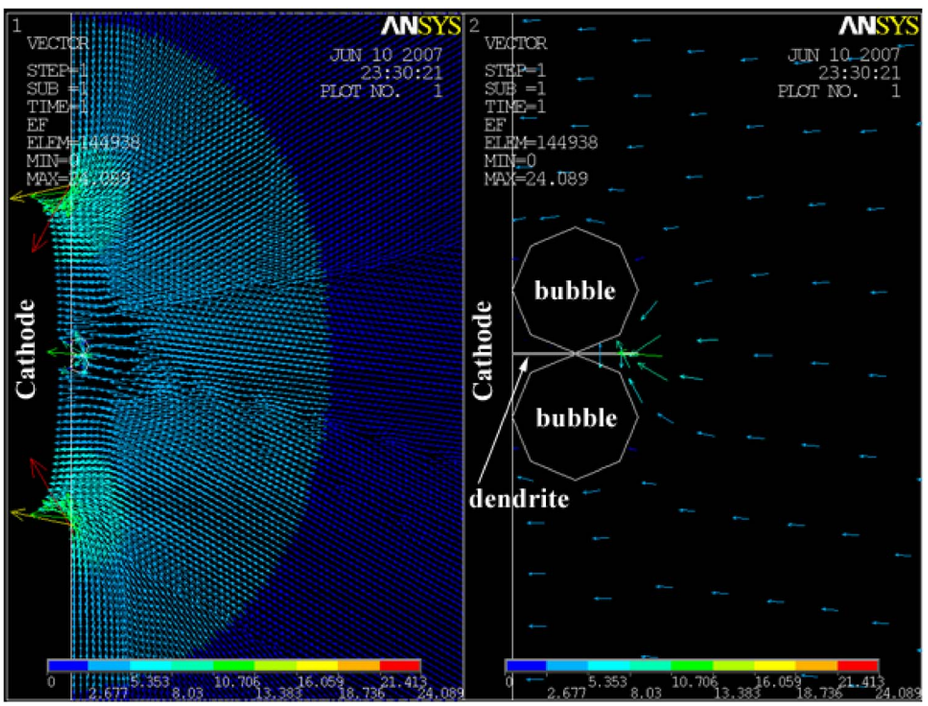

Figure 11. (Color online) Electric-field distribution between the zinc anode and the cathode for a dendrite constricted by bubbles. A closer view is shown on the right side.

mode, the zinc deposit remained fern-shaped dendrite throughout the entire potentiostatic-mode deposition. The morphology transition in the galvanostatic mode from the fern-shaped dendrite with a major stem in the axial direction to the dense-branching observed in Fig. 6 can thus be attributed to the change in the bubble formation rate.

Figure 10 shows a schematic diagram for the formation of fern-shaped dendrites. Once an existing dendrite is surrounded by a couple of hydrogen bubbles, the concentration of zinc ions can be divided into two zones, a Zn^{2+}-depleted zone in the space between the two bubbles and a zone with the original Zn^{2+} concentration outside them. The Zn^{2+} concentration difference between these two zones can cause local convection[40,41] (Fig. 10a), replenishing the zinc ions necessary for the growth of the main stem of the fern-shaped dendrites. The creation of hydrogen bubbles suppresses the lateral growth of fern-shaped dendrites, while a fast tip growth is promoted by the concentrated electric field (Fig. 10b and c). When the main stem outgrows the surrounding hydrogen bubbles, its side branches start to split, leading to the appearance of fern-shaped dendrites (Fig. 10d). Figure 10e is an enlarged X-ray image taken from Fig. 6 showing an example of the fern-shaped dendrite.

To better examine this phenomenon, a simple electric field analysis was performed. Figure 11 shows the electric-field distribution across the zinc anode and cathode with a dendrite constricted by bubbles. The electric field is not only concentrated on the dendrite tip but also distributed on the dendrite stem. This causes the growth of long dendrite stems and side branches. In the case of galvanostatic plating, the lateral growth gradually dominates the overall ramified formation because the potential drops as the plating continues, reaching values too low for sufficient bubble formation for the growth of fern-shaped dendrites. As a result, in the galvanostatic mode the fern-shaped dendrites evolve to a more-compact ramified deposit as the plating continues.

Conclusion

The tendency to eventually produce densified growth with potential dropping below the value needed for hydrogen-bubble formation makes the galvanostatic mode less suitable than potentiostatic plating for applications requiring large surface areas. Indeed, fern-shaped dendrites have much larger surface areas than the dense-branching structure. These interlaced dendrites, once collapsed after removal from the electrolyte, result in a porous structure. Zinc electrodeposits composed of fern-shaped dendrites have been shown to possess large electrochemically active surface areas[13] ideal for Zn–air batteries. Our results suggest that this type of fabrication can be achieved by controlling the hydrogen-bubble formation, which is directly related to the applied potential rather than to the current density.

This practical conclusion can lead to interesting applications in plating technology, transforming bubbles from negative elements to

potentially useful tools. In general, our results stress the importance of real-time study to fully understand electroplating and to identify new ways to exploit its potential capabilities.

Acknowledgments

This work was supported by the National Science Council (Taiwan), by the Academia Sinica, by the National Nanoscience and Nanotechnology Program (Taiwan), by the Creative Research Initiatives (Functional X-ray Imaging) of MOST/KOSEF (Korea), by the Swiss Fonds National de la Recherche Scientifique, and by the EPFL (Switzerland).

Academia Sinica assisted in meeting the publication costs of this article.

References

1. D. H. Coleman, B. N. Popov, and R. E. White, *J. Appl. Electrochem.*, **28**, 889 (1998).
2. M. Monev, L. M. Mirkova, I. Krastev, H. Tsvetkova, S. Rashkov, and W. Richtering, *J. Appl. Electrochem.*, **28**, 1107 (1998).
3. W. L. Tsai, P. C. Hsu, Y. Hwu, C. H. Chen, L. W. Chang, J. H. Je, H. M. Lin, A. Groso, and G. Margaritondo, *Nature (London)*, **417**, 319 (2002).
4. H. C. Shin and M. Liu, *Chem. Mater.*, **16**, 5460 (2004).
5. J. W. Long, L. R. Qadir, R. M. Stroud, and D. R. Rolison, *J. Phys. Chem. B*, **105**, 8712 (2001).
6. J. S. Sakamoto and B. Dunn, *J. Mater. Chem.*, **12**, 2859 (2002).
7. G. Q. Zhang, X. G. Zhang, and H. L. Li, *J. Solid State Electrochem.*, **10**, 955 (2006).
8. K. Kinoshita, X. Song, K. Kim, and M. Inaba, *J. Power Sources*, **81–82**, 170 (1999).
9. C. C. Yang and S. J. Lin, *J. Power Sources*, **112**, 174 (2002).
10. Y. Sawada, A. Dougherty, and J. P. Gollub, *Phys. Rev. Lett.*, **56**, 1260 (1986).
11. D. Grier, E. Ben-Jacob, R. Clarke, and L. M. Sander, *Phys. Rev. Lett.*, **56**, 1264 (1986).
12. P. P. Trigueros, J. Claret, F. Mas, and F. Sagues, *J. Electroanal. Chem. Interfacial Electrochem.*, **312**, 219 (1991).
13. C. M. Lopez and K. S. Choi, *Langmuir*, **22**, 10625 (2006).
14. J.-N. Chazalviel, *Phys. Rev. A*, **42**, 7355 (1990).
15. V. Fleury, J.-N. Chazalviel, and M. Rosso, *Phys. Rev. Lett.*, **68**, 2492 (1992).
16. V. Fleury, J.-N. Chazalviel, and M. Rosso, *Phys. Rev. E*, **48**, 1279 (1993).
17. C. Livermore and P. Z. Wong, *Phys. Rev. Lett.*, **72**, 3847 (1994).
18. D. P. Barkey, D. Watt, Z. Liu, and S. Raber, *J. Electrochem. Soc.*, **141**, 1206 (1994).
19. Y. Hwu, W. L. Tsai, A. Groso, G. Margaritondo, and J. H. Je., *J. Phys. D*, **35**, R105 (2002).
20. G. Margaritondo, Y. Hwu, and J. H. Je, *Riv. Nuovo Cimento*, **27**, 7 (2004).
21. Y. Hwu, J. H. Je, and G. Margaritondo, *Nucl. Instrum. Methods Phys. Res. A*, **551**, 108 (2005).
22. W. L. Tsai, P. C. Hsu, Y. Hwu, J. H. Je, Y. Ping, H. O. Moser, A. Groso, and G. Margaritondo, *Nucl. Instrum. Methods Phys. Res. B*, **199**, 436 (2003).
23. R. Meuli, Y. Hwu, J. H. Je, and G. Margaritondo, *Eur. J. Radiol.*, **141**, 550 (2004).
24. W. L. Tsai, P. C. Hsu, Y. Hwu, C. H. Chen, L. W. Chang, J. H. He, A. Groso, and G. Margaritondo, *Nucl. Instrum. Methods Phys. Res. B*, **199**, 451 (2003).
25. S. K. Seol, J. M. Yi, X. Jin, C. C. Kim, J. H. Je, W. L. Tsai, P. C. Hsu, Y. Hwu, C. H. Chen, L. W. Chang, et al., *Electrochem. Solid-State Lett.*, **7**, C95 (2004).
26. N. D. Nikolic, K. I. Popov, L. J. Pavlovic, and M. G. Pavlovic, *J. Electroanal. Chem.*, **588**, 88 (2006).
27. E. Ben-Jacob, G. Deutscher, P. Garik, N. D. Goldenfeld, and Y. Lareah, *Phys. Rev. Lett.*, **57**, 1903 (1986).
28. E. Ben-Jacob, P. Garik, and D. Geier, *Superlattices Microstruct.*, **3**, 599 (1987).
29. D. R. Rolison and B. Dunn, *J. Mater. Chem.*, **11**, 963 (2001).
30. F. Beck and P. Ruetschi, *Electrochim. Acta*, **45**, 2467 (2000).
31. J. Goldstein, I. Brown, and B. Koretz, *J. Power Sources*, **80**, 171 (1999).
32. B. O'Regan, D. T. Schwartz, S. M. Zakeeruddin, and M. Gratzel, *Adv. Mater. (Weinheim, Ger.)*, **12**, 1263 (2000).
33. Y. Liu, S. Zha, and M. Liu, *Adv. Mater. (Weinheim, Ger.)*, **16**, 256 (2004).
34. H. S. Liu, C. J. Song, Y. H. Tang, J. L. Zhang, and J. J. Zhang, *Electrochim. Acta*, **52**, 4532 (2007).
35. S. Baik, H. S. Kim, M. H. Jeong, C. S. Lee, J. H. Je, Y. Hwu, and G. Margaritondo, *Rev. Sci. Instrum.*, **75**, 4355 (2004).
36. G. L. M. K. S. Kahanda and M. Tomkiewicz, *J. Electrochem. Soc.*, **136**, 1497 (1989).
37. D. Pletcher and F. C. Walsh, *Industrial Electrochemistry*, 2nd ed., Chapman and Hall, London (1993).
38. S. S. Zumdahl, *Chemical Principles*, p. 487, Houghton Mifflin Company, Boston, MA (2002).
39. J. R. Bruyn, *Phys. Rev. E*, **56**, 3326 (1997).
40. L. J. J. Janssen and J. G. Hoogland, *Electrochim. Acta*, **15**, 1013 (1970).
41. F. Ajersch, D. Mathieu, and D. L. Piron, *Can. Metall. Q.*, **24**, 53 (1985).